communications earth & environment

ARTICLE

https://doi.org/10.1038/s43247-024-01234-9 OPEN

Detection of thin film phase transformations at high-pressure and high-temperature in a diamond anvil cell

Meryem Berrada[1,2], Genzhi Hu[3], Dongyuan Zhou[2], Siheng Wang[1], Phuong Q. H. Nguyen[1,4], Dongzhou Zhang[1,4], Vitali Prakapenka[4], Stella Chariton[4], Bin Chen[1], Jie Li[2] & Jason D. Nicholas[3,5]✉

Quantifying how grain size and/or deviatoric stress impact $(Mg,Fe)_2SiO_4$ phase stability is critical for advancing our understanding of subduction processes and deep-focus earthquakes. Here, we demonstrate that well-resolved X-ray diffraction patterns can be obtained on nano-grained thin films within laser-heated diamond anvil cells (DACs) at hydrostatic pressures up to 24 GPa and temperatures up to 2300 K. Combined with well-established literature processes for tuning thin film grain size, biaxial stress, and substrate identity, these results suggest that DAC-loaded thin films can be useful for determining how grain size, deviatoric stress, and/or the coexistence of other phases influence high-pressure phase stability. As such, this novel DAC-loaded thin film approach may find use in a variety of earth science, planetary science, solid-state physics, and materials science applications.

[1] Hawaii Institute of Geophysics and Planetology, University of Hawaii at Manoa, Honolulu, HI, USA. [2] Earth and Environmental Sciences Department, University of Michigan, Ann Arbor, MI, USA. [3] Chemical Eng. & Materials Science Department, Michigan State University, East Lansing, MI, USA. [4] Center for Advanced Radiation Sources, The University of Chicago, Chicago, IL, USA. [5] Fraunhofer USA Center Midwest, Coatings and Diamond Technology Division, East Lansing, MI, USA. ✉email: jdn@msu.edu

With increasing depth, the olivine-structured α-$(Mg,Fe)_2SiO_4$ within the Earth's mantle transition zone (MTZ) transforms into spinelloid-structured β-$(Mg,Fe)_2SiO_4$, which then transforms into spinel-structured γ-$(Mg,Fe)_2SiO_4$[1–3]. However, the spatial distributions over which these mantle transition zone phase transformations occur in subducting oceanic crust, and whether they cause deep-focus earthquakes, has remained controversial[4–12]. Some of this controversy has focused on subducting slab water contents and the impact that water has on $(Mg,Fe)_2SiO_4$ phase stability, transformation kinetics, and transformation mechanisms[13–16]. Unfortunately, less attention has been paid to how extremely small grain size and/or extremely large deviatoric stress impact $(Mg,Fe)_2SiO_4$ phase stability. Specifically, past experimental studies on micro-grained samples under low-to-moderate levels of deviatoric stress have shown that conversion between the three Mg_2SiO_4 polymorphs (α (forsterite), β (wadsleyite), and γ (ringwoodite)) occurs via either (1) a second-phase nucleation and growth mechanism, or via (2) displacive shear transformations that occur either directly between phases or proceed through an intermediate poirierite (ε*) phase[16–18]. This first "inter-crystalline" mechanism (so named because the phase transformation starts "between the grains" due to the lower nucleation barrier for second-phase nucleation at the grain boundaries compared to the grain interior) is favored at high temperatures, small reactant grain sizes, and/or small deviatoric stress[19–23]. The opposite is true for the "intra-crystalline" shear mechanism[19–23]. These temperature, grain size, and deviatoric stress dependencies have been justified by arguments that (a) higher temperatures are needed to enable the bulk diffusion required in the inter-crystalline mechanism[20], (b) nucleation and growth on grain boundaries is fast enough to consume small grains before the intra-crystalline transformation dominates[19], and (c) deviatoric stress promotes the intra-crystalline mechanism by increasing the dislocation density[22]. However, despite much work showing how grain size and/or deviatoric stress impact Mg_2SiO_4 phase transformation reaction pathways and kinetics[16–23], little to no attention has been paid to how nano-grain sizes and/or large deviatoric stress impact Mg_2SiO_4 polymorph thermodynamic stability.

This is problematic because large deviatoric stresses up to ~1 GPa have been predicted to exist within subduction zones[24–26], and nano-grained rocks (mylonites) are known to occur in high-shear zones due to deformation and/or shear-induced recrystallization[27]. In addition, past studies have shown that $(Mg,Fe)_2SiO_4$ phase transformations can cause grain size reductions[28–30]. In particular, Rosa et al.[28] reported that "both the α→β and β→γ transformation induce significant reductions of the mean sample grain size of up to 90%." Further, Ohuchi et al.[31] found that $(Mg,Fe)_2SiO_4$ samples made up of ~15 μm diameter olivine grains formed pockets of 20–1000 nm diameter olivine and wadsleyite grains under mantle transition zone pressure-temperature (P-T) conditions that facilitated throughgoing faulting capable of producing "intense acoustic emissions". Hence, it seems possible that, despite the tendency of nano-grained systems to coarsen over geologic timescales, shear-induced and/or phase-transformation-induced grain size reductions are able to generate, regenerate, and/or otherwise maintain nano-grained $(Mg,Fe)_2SiO_4$ in actively subducting slabs at MTZ depths.

There are several reasons to suspect that nano-sized and/or deviatorically-stressed $(Mg,Fe)_2SiO_4$ grains might have different polymorph P-T stability limits than the large, "hydrostatically-stressed" $(Mg,Fe)_2SiO_4$ grains found in most other parts of the Earth's mantle. First, there are many examples of grain size impacting phase stability in other material systems. For instance, in TiO_2 it has been shown that small grain sizes can thermodynamically stabilize the photo-catalytically active anatase polymorph, instead of the rutile polymorph found in larger grains at identical surrounding pressure/temperature conditions[32–34]. Similarly, by forcing $BaTiO_3$ into a cubic, instead of a tetragonal crystal structure, grain size reductions can eliminate the $BaTiO_3$ ferroelectric behavior used for capacitor, actuator, and sensor applications[35–37].

Second, past thermodynamic derivations demonstrate how grain size reductions can shift phase boundaries[38]. Specifically, the impact of grain size on thermodynamic stability can be approximated via the Young-LaPlace equation:

$$\Delta P = 2\Gamma/r \quad (1)$$

which shows that, on account of the surface energy (Γ), spherical particles of a given radius (r) (even those outside a DAC or thin film) experience an additional pressure (ΔP) compared to that experienced by infinitely large particles under the same surrounding pressure and temperature conditions[38–40]. For instance, according to Eq. (1), a spherical, 30-nm-diameter forsterite grain with a (101) surface tension of 1.8 J/m^2 that is assumed to represent the average surface tension of all the grain's exposed surfaces[41] would be under a very modest ΔP of 0.2 GPa that is within the pressure determination accuracy of most high-pressure diamond anvil cell (DAC) experiments[42]. In contrast, a spherical, 7-nm-diameter forsterite grain with an assumed Γ=1.8 J/m^2 would be under a ΔP of 1.0 GPa that might be enough to meaningfully shift the surrounding pressures and/or temperatures at which phase transformations occur. Hence, given that 20-nm-diameter $(Mg,Fe)_2SiO_4$ grains have already been observed to form in laboratory experiments[31], its seems likely that grain sizes small enough to impact $(Mg,Fe)_2SiO_4$ phase stability may occur in some portions of actively subducting slabs.

Third, in addition to grain size, it is well known that deviatoric stress can alter polymorph thermodynamic stability. This is commonly observed in epitaxial thin films where, to save the energy of a film-substrate grain boundary, it is energetically favorable for a thin film's lattice planes to biaxially strain so that they completely align (or if that is too difficult by introducing the occasional edge dislocation to mostly align) with those of the underlying substrate[43]. This leads to an epitaxial film stress that can be up to several gigapascals in magnitude[44] and can stabilize polymorphs different than those predicted by the equilibrium bulk phase diagram[45–47]. Similarly, the multi-GPa[48,49] biaxial stresses that can be generated in non-epitaxial thin films via mechanisms such as grain impingement during film growth[50], post-deposition thin film crystallization[51], film-substrate coefficient of thermal expansion mismatch of thin films deposited at one temperature and tested at another[50], and/or film-substrate compressibility mismatch of thin films deposited at one pressure and tested at another[52], may also meaningfully impact thermodynamic phase stability.

Hence, the objective of the present work was to evaluate the viability of a new "DAC-loaded thin film" mineral physics approach to quantify how grain size, deviatoric stress, and/or the coexistence of other phases impact high-pressure phase stability. Although thin films have been used previously to probe the ambient, high-temperature, and/or high-pressure behavior of bulk materials[53,54], they have never been considered as representative of deep-Earth materials. This seems like a missed opportunity because, as detailed previously, nano-grained and/or deviatoric stresses materials may occur in subducting slabs. In addition, it should be possible to (1) use the well-known thin film mean grain size modulation techniques found in the literature (alteration of the thin deposition temperature[55], the thin film deposition atmosphere[56], the post-deposition annealing

schedule[57], etc.) to produce thin films with ~1–1000 nm mean grain sizes similar to those possible in subducting slabs, and (2) use the aforementioned thin film biaxial stress modulation techniques[50–52] to subject DAC-loaded thin films to well-controlled complex (i.e., deviatoric + hydrostatic) stress states similar to those in subducting slabs. Further, the film composition and substrate flexibility offered by the pulsed laser deposition (PLD)[43] thin film deposition technique utilized here should allow facile examinations of how sample stoichiometry, substrate composition, and/or substrate orientation alter phase stability. Lastly, the ability to examine the phase stability of thin films (which can support either tensile or compressive deviatoric stresses up to several GPa in magnitude)[44,48,49,58] in diamond anvil cells (which have been shown capable of producing "quasi-hydrostatic" stresses up to several terra-pascals in magnitude)[59] would also allow materials to be studied under complex stress states previously-unachievable in the laboratory (such as under large deviatoric stresses above the ~100 GPa hydrostatic pressure limits of existing D-DIA multi-anvils[60], etc.).

Unfortunately, the small sample volumes and crystallographic preferred orientation commonly exhibited by thin films[43] make it difficult to use X-ray diffraction (XRD) to perform phase stability studies on DAC-loaded thin films. Hence, the present work evaluated the hypothesis that well-resolved DAC-loaded thin film XRD signals could be obtained as a function of temperature and/or pressure using third-generation synchrotron X-ray sources and large area XRD detectors.

Results and discussion

The high-pressure XRD measurements performed here captured distinct, well-resolved DAC-loaded thin film XRD patterns for forsterite, wadsleyite, ringwoodite, akimotoite, and/or bridgmanite at hydrostatic pressures ranging from 0.1 to 24 GPa and temperatures ranging from 298 to 2300 K. Specifically, Fig. 1 shows select room-temperature and high-temperature 2D XRD patterns collected within pressurized DACs on ~400 nm thick, non-epitaxial Mg_2SiO_4 films made up of ~30 nm sized grains atop MgO single-crystal substrates (see Section 4 for details on the sample fabrication and testing procedures). Multiple thin film XRD peaks were discernible at each pressure, and the different angular and radial positions of the thin film XRD peaks made it clear that five different thin film phases (forsterite, wadsleyite, ringwoodite, akimotoite, and bridgmanite) were observed. The radially-integrated two-theta XRD plots (obtained from 2D XRD patterns like those in Fig. 1) are shown in Fig. 2. In addition, Fig. 2 also contains insets of portions of the 2D XRD patterns taken at the same pressure as the two-theta XRD pattern in each row (to illustrate how resolved certain phase-identifying peaks were). In Fig. 3a, the identified phases as a function of pressure and temperature are reported, and in Fig. 3b they are compared to literature reports of the phase boundaries of bulk Mg_2SiO_4 at low deviatoric stress.

At ambient temperature, the Mg_2SiO_4 thin films retained their forsterite structure up to 26.5 GPa. In contrast and perhaps not surprising due to the fast kinetics enabled by a small ~30 nm mean grain size providing many nucleation sites, upon heating to ~1000 K at each of the high pressures analyzed here, the forsterite films adopted the equilibrium phases indicated by the simulated bulk phase diagram of Hernandez et al.[61] (denoted by the solid lines in Fig. 3). When quenched from high temperature, the thin films retained the last structure observed at high temperature at a given pressure.

Figures 2 and 3 show that from ~8 to 14 GPa, the thin film Mg_2SiO_4 phase behavior from ~1000 to 2000 K was largely consistent with that reported previously in the literature for conventional samples (i.e., micro-grained samples under nominally low amounts of deviatoric stress). Specifically, with additional heating above 1000 K at 9.3 and 11.5 GPa, the thin films retained their forsterite structure, in agreement with previous literature reports. Furthermore, at 13.7 GPa, the wadsleyite that had formed from the original forsterite at this pressure transformed back into forsterite at ~1300 K. As shown by comparing the Fig. 2 forsterite peak intensities with those for a randomly oriented polycrystal indicated by the percentage numbers in Figure S1 of Supplementary Materials, this regenerated forsterite exhibited crystallographic preferred orientation that was different from the original forsterite film. As shown in Fig. 3, the observed thin film wadsleyite-to-forsterite phase transformation pressure and temperature were similar to some previous reports[62–65], but different from others[61,66,67]. It is possible that some of the discrepancies that exist between the various literature reports may be related to uncertainty in the high-temperature pressure scale used in previous literature measurements, and the associated *P-T* error bars. Curiously, the pressure and temperature of the wadsleyite-to-forsterite transition reported in the previous literature does not correlate with the characterization approach used in those studies.

In contrast to the behavior at lower pressure, Figs. 2, 3 and S2 show that at ~18 GPa the thin film Mg_2SiO_4 phase behavior was dramatically different than that reported previously for conventional samples. In agreement with the literature, with heating to ~1000 K at ~18 GPa, the originally-forsterite-structured Mg_2SiO_4 thin films transformed into ringwoodite. However, it took until ~1900 K for this thin film ringwoodite to transform into wadsleyite. This transformation is clearly shown by the disappearance of the ringwoodite 220 peak, and the appearance of the wadsleyite 080 and 112 peaks at ~1900 K in Figs. 2 and S2. At ~18 GPa, this ringwoodite-to-wadsleyite phase transformation occurred at ~1900 K, which is ~500 K higher than the previously reported experimental values[62,64,68,69], and ~300 K lower than temperature-uncorrected Density Functional Theory results[61].

Figures 2 and 3 show that at ~19 GPa the thin film Mg_2SiO_4 phase behavior between ~1000 K and 2000 K was similar to that reported in the literature for conventional samples. Specifically, at ~19.5 GPa and ~20 GPa, the thin film Mg_2SiO_4 contained ringwoodite over all tested temperatures from ~1000 to 2000 K, consistent with the conventional Mg_2SiO_4 phase diagram.

Figures 2 and 3 also show that at ~23 GPa and ~1000 K the sample exhibited (1) $MgSiO_3$ akimotoite XRD peaks and (2) MgO XRD peaks that were likely from both the substrate and from the chemical breakdown of the thin film Mg_2SiO_4. This behavior agreed with Hernandez et al.'s Mg_2SiO_4 simulations[61], as did conversion of the akimotoite into bridgmanite observed here at ~1454 K and ~23 GPa. However, the observation of akimotoite + periclase from ~1000 to 1454 K at 23 GPa disagreed with past experimental studies which have either directly-observed[70] or assumed[62,71,72] that ringwoodite is stable at these P-T conditions. The results here, along with possible discrepancies in previous studies resulting from the use of Au versus Pt versus MgO pressure sensors[72], the observation of a metastable akimotoite + periclase assemblage near the edges of Hernandez et al.'s akimotoite + periclase stability window[73], past suggestions that the akimotoite to bridgmanite transition is seismically relevant[74], the possibility of slow kinetics resulting from the larger grain sizes used in previous studies[70], and the removal of the MgO nucleation barrier here caused by the use of a MgO substrate, suggest that a previously-unconfirmed, Earth-relevant akimotoite + periclase phase field may exist in the Mg_2SiO_4 phase diagram. However, additional thin film + DAC experiments performed as a function of grain size, deviatoric-stress, substrate-identity, and water content are needed before firm conclusions can be drawn.

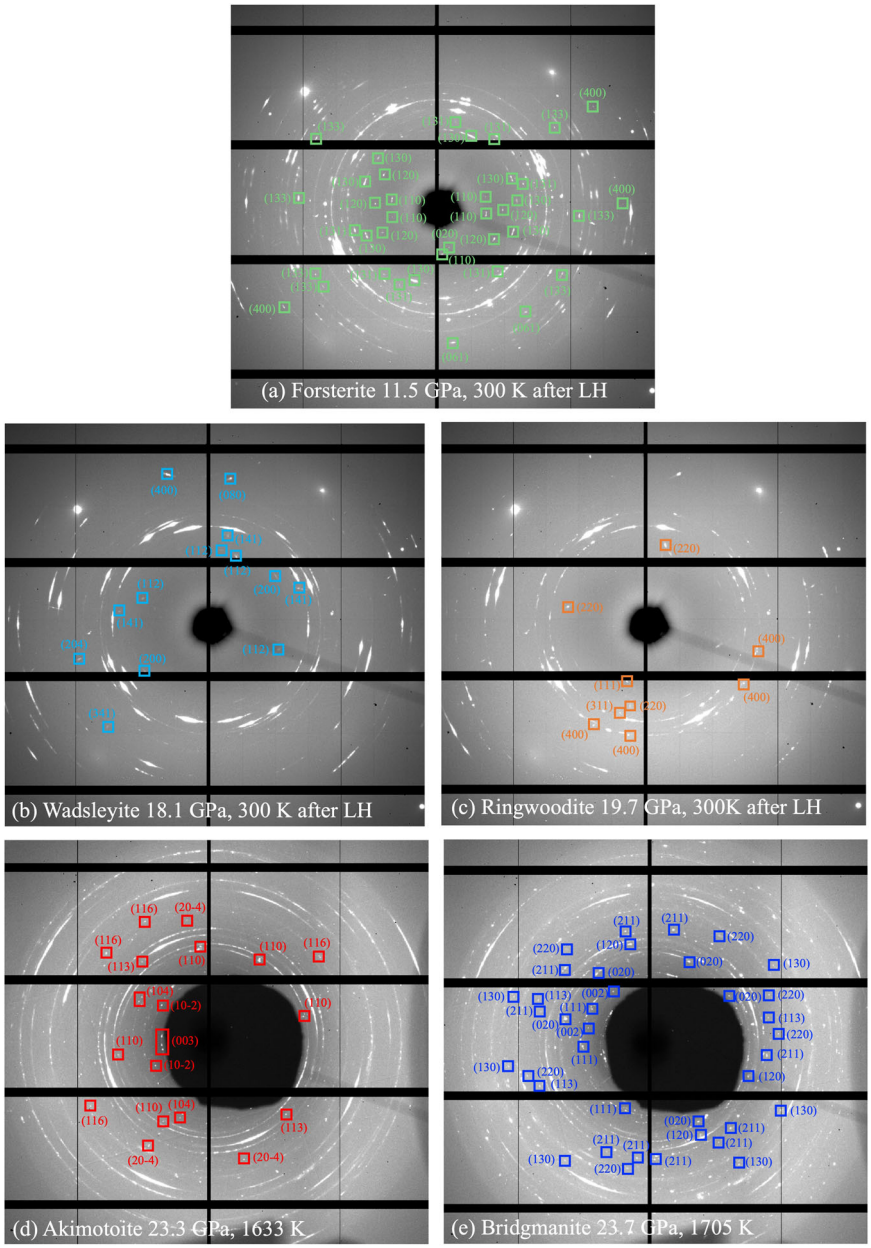

Fig. 1 Representative 2D XRD patterns from DAC-loaded Mg_2SiO_4 | MgO samples. a Forsterite (green squares) at 11.5 GPa and 300 K after LH (Laser Heating), **b** wadsleyite (light blue squares) at 18.1 GPa and 300 K after LH, **c** ringwoodite (orange squares) at 19.7 GPa and 300 K after LH, **d** akimotoite (red squares) at 23.3 GPa and 1436 K, and **e** bridgmanite (dark blue squares) at 23.7 GPa and 1705 K. The black circular region at the center of each 2D pattern corresponds to the X-ray beam stop. Images (**d**) and (**e**) were taken during LH which required a larger X-ray beam stop to adsorb scattering from the laser heating mirror. The Forsterite peaks were identified from those reported in Smyth and Hazen (1973)[82], the wadsleyite peaks from those in Hazen et al. (2000)[83], the ringwoodite peaks from those in Sasaki et al. (1982)[84], the akimotoite peaks from those in Horiuchi et al. (1982)[85], and the bridgmanite peaks from those in Sugahara et al. (2006)[86].

It is important to note that the water content in the films analyzed here was not controlled, or analyzed, even though tens of ppm's of water have been shown to impact $(Mg,Fe)_2SiO_4$ phase stability[13,14]. Further, a reduction in the synchrotron XRD thin film signal intensity that occurred over the five months between Run #1 and #2 suggests that the samples may have changed their water content between synchrotron analyses. These unknown/uncontrolled water contents may lead some readers to question whether the phase boundary shifts observed here were instead caused by water impurities. However, this seems unlikely since the water-enhanced transformation rates shown in previous literature[13,14] imply that water impurities should have pushed both the forsterite-to-wadsleyite and the ringwoodite-to-wadsleyite phase transformations to lower temperatures at a given pressure, not the higher temperatures at a given pressure observed here.

Similarly, while thermal expansion is inherently accounted for by the high-temperature equation of state of platinum, the consideration of thermal pressure through the fitting of an equation of state to each phase was not incorporated into this work. The primary focus of this study was the detection of thin film phases (and the transitions between them) not collection of the multiple XRD patterns required for an accurate equation of state. It should be noted that the behavior of the thermal pressure in forsterite is

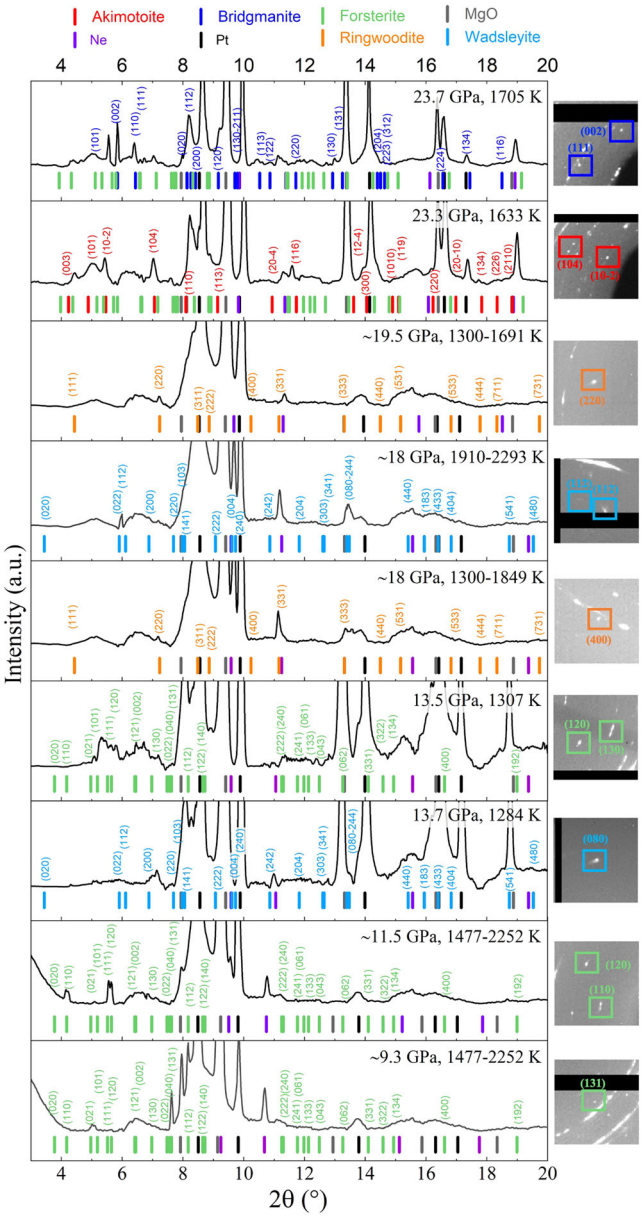

Fig. 2 XRD measurements of thin film Mg_2SiO_4 on MgO at high pressure and temperature. Strong, phase-identifying peaks are shown to the right of the corresponding XRD pattern. The platinum peaks are compared to those from Wyckoff (1963)[87], the neon peaks to those from de Smedt et al. (1930)[88], and the periclase peaks to those from Hazen (1976)[89]. The temperature range listed in each XRD pattern refers to the range over which the XRD patterns were summed to amplify the thin film signal intensity. These XRD measurements were collected using a wavelength of 0.3344 Å.

reported to increase linearly at high temperatures and decrease with pressure[75]. If wadsleyite behaves similarly, then observation of the wadsleyite-to-ringwoodite phase transformation occurring at higher temperatures than past reports might be partially explained by thermal pressure. However, the large magnitude of the observed wadsleyite-to-ringwoodite phase transformation temperature shift (~500 K at ~18 GPa), and the fact that any thermal pressure present did not dramatically shift the other thin film Mg_2SiO_4 phase transformations, suggests that thermal pressure may not be the sole cause of the dramatic shift in the wadsleyite-to-ringwoodite phase transformation. Although future work is needed to confirm the present results and identify the active mechanisms, the phase boundary shifts observed here are consistent with thin film forsterite and wadsleyite having their chemical potentials by a similar, large amount (relative to the other phases found in the Mg_2SiO_4 system).

Conclusions

This work demonstrated, for the first time, that (1) well-resolved XRD signals could be obtained on thin films within pressurized, laser-heated diamond anvil cells, and (2) high-pressure phase transformations could be successfully monitored in situ within a DAC. Specifically, the thin film Mg_2SiO_4 forsterite-to-wadsleyite transformation was observed at *P-T* conditions similar to those reported previously for micro-sized Mg_2SiO_4 under low-to-moderate amounts of deviatoric stress. The *P-T* conditions of the thin film Mg_2SiO_4 (akimotoite+periclase)-to-(bridgmanite +periclase) phase transformation, and the thin film Mg_2SiO_4 (akimotoite+periclase) phase stability field, agreed with past simulation results, but disagreed with past experimental results. The *P-T* conditions of the thin film Mg_2SiO_4 wadsleyite-to-ringwoodite transformation occurred ~300 K lower at ~18 GPa (~1 GPa lower at 1900 K) than previous simulation results, but ~500 K higher at ~18 GPa (~2.5 GPa lower at 1900 K) than previous experimental reports. Future work is needed to confirm the thin film observations, identify the source of any discrepancies between bulk and thin film behavior, and explore their geological significance.

The present results also demonstrate the viability of future DAC-loaded thin film experiments aimed at understanding how grain size, deviatoric stress, and/or the coexistence of other phases alter high-pressure phase stability. It is expected that the DAC-loaded thin film approach outlined here will be useful for a variety of earth science, planetary science, solid-state physics, and materials science applications.

Methods

The non-epitaxial Mg_2SiO_4 thin films used here were produced via pulsed laser deposition (PLD) onto one-side polished, 25 mm diameter, ~200-micron-thick, (100)-oriented MgO single-crystal substrates (Crystec, Berlin, Germany) heated to 850 K in 9 mTorr of O_2 and placed 70 mm from a Mg_2SiO_4 target irradiated with a 248 nm KrF excimer laser pulsed 54,000 times for 20 ns every 0.1 s with a nominal 270 mJ/pulse laser energy that, after 55% of optical loss and focusing down to 2.0 mm^2, produced a fluence of 6.1 J/cm^2 on the Mg_2SiO_4 target. The Mg_2SiO_4 target used for PLD was produced by pressing ~9.5 g of Mg_2SiO_4 powder (Alfa Aesar; Ward Hill, MA, USA) to ~12 MPa in a 38 mm stainless steel die and firing the resulting powder pellet at 1673 K in air for 4 h, using nominal 5 °C/min heating and cooling rates. As this yielded an insufficient target relative density of only ~63%, the target was fired again to 1773 K in air for 4 h, using nominal 5 °C/min heating and cooling rates. Unfortunately, since this only increased the pellet relative density to 73%, the target was heated a final time to 1873 K for 8 h in air, using nominal 5 °C/min heating and cooling rates, to produce an 89% dense Mg_2SiO_4 target. The target was then ground down to a thickness of 2.4 mm and a diameter of 25.2 mm with down to P4000 SiC sandpaper, and bonded to a ~3.5 mm thick, 25.4 mm diameter Cu backing plate.

After thin film deposition, the Mg_2SiO_4 | MgO samples were heated to 1473 K for 1 h in air, with nominal 3 °C/min heating and cooling rates, to crystallize the Mg_2SiO_4 and re-equilibrate its oxygen content with air. These air-annealed samples were used for all subsequent analyses.

The crystal structure of the Mg_2SiO_4 thin films were characterized via grazing angle X-ray diffraction collected using a

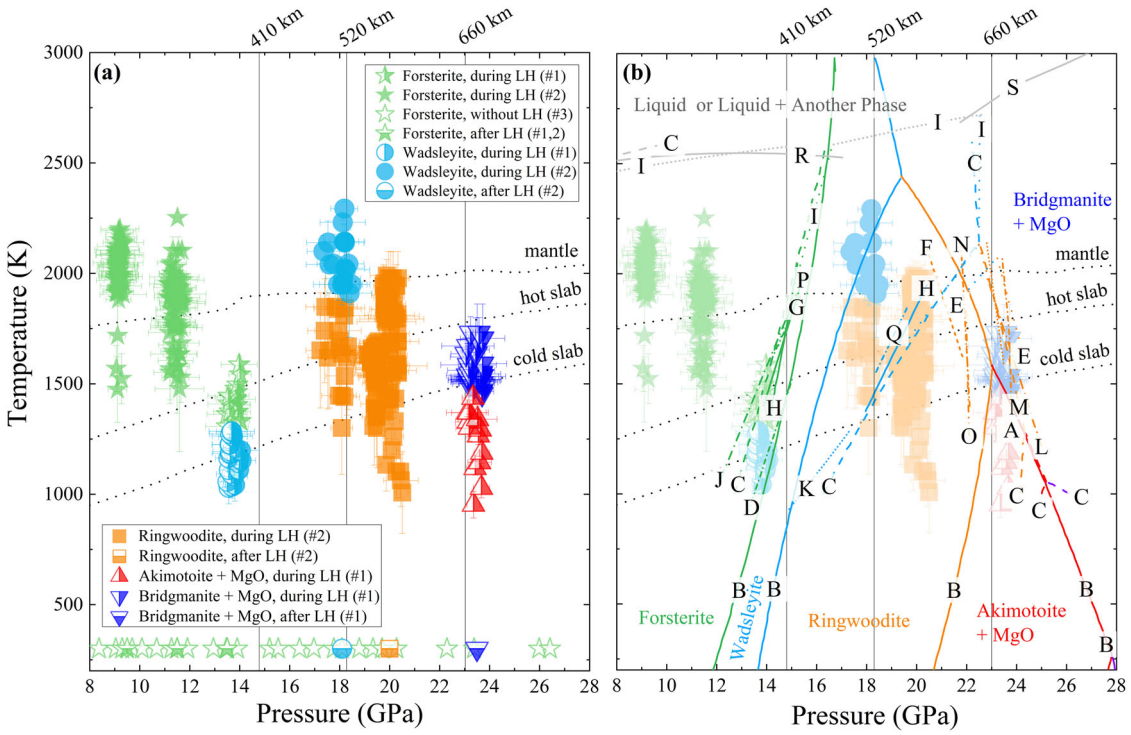

Fig. 3 Thin film Mg_2SiO_4 phase stability summary and literature comparison. Thin film Mg_2SiO_4 phase stability (**a**) observed here during Runs #1 (13.5 and 23.5 GPa vs. temperature), #2 (9.5, 11.5, 18, and 19.5 GPa vs. temperature), and #3 (8.3 to 26.5 GPa at 300 K), and **b** compared with literature studies: A[70], B*[61], C[62], D[66], E[90], F[91], G[63], H*[64], I[92], J[67], K[68], L[71], M[72], N[93], O[94], P*[65], Q[69], R*[95], and S*[96]. The * citation notations in the previous sentence and the solid phase boundary lines in the phase diagram denote simulated results. The mantle, hot slab and cold slab temperature profiles, in addition to the pressures expected at 410, 520, and 660 km[64,97], are displayed for comparison. The green lines correspond to the breakdown of forsterite, the light blue lines to that of wadsleyite, the orange lines to that of ringwoodite, the red lines to that of akimotoite, the gray lines to the onset of melting, and the short purple lines (in the lower right corner) to the transition of stishovite + periclase to bridgmanite + periclase. The pressure uncertainty bars are due to uncertainty in the volume of platinum. The temperature uncertainty bars are due to the deviation between the temperatures recorded during LH on each side of the sample, and temporal variations in the local temperature measurements.

SmartLab X-Ray Diffractometer (Rigaku Americas Corp., The Woodlands, TX, USA) operated with a constant 2° angle of incidence, a 2.59°/min scan speed, and Cu K_α radiation ($\lambda = 1.5406$ Å). Figure S1 shows that Mg_2SiO_4 films produced with the approach described here were comprised of phase-pure, highly crystalline forsterite. As highlighted by the difference in the Figure S1 XRD peak intensity ratios observed here compared to those observed for random polycrystals in JCPDS PDF# 00-004-0768, the forsterite thin films produced here exhibited crystallographic preferred orientation, a common occurrence in thin films[43,55,76]. Thankfully, even with this crystallographic preferred orientation, the position and high number of XRD peaks (>7) definitively indicated that forsterite was the only crystalline phase present in the thin films produced here. Room-temperature instrument-corrected peak broadening analyses performed using the Figure S1 grazing angle XRD results (and those obtained at the synchrotron) indicated that the average forsterite grain size was ~30 nm and the 300 K forsterite biaxial film stress was ≤0.1 GPa. Unfortunately, elevated temperature in-DAC XRD-based determinations of the thin film grain size and/or thin film biaxial stress levels were not possible due to (1) the weak elevated-temperature thin film XRD signals, and (2) the difficulty in sampling an in-plane thin film strain with an out-of-plane XRD geometry.

To determine the film thickness, Mg_2SiO_4 | MgO sample fragments were prepared for focused ion beam-scanning electron microscopy (FIB-SEM) analysis by embedding them in Epofix epoxy (Buehler Inc., Lake Bluff, IL, USA) and consecutively grinding them with 240, 400, 800, and finally 1200-grit SiC sandpaper. The FIB-SEM sample was then polished with 9 µm, 3 µm, and finally 1 µm polycrystalline diamond polishing agent. FIB-SEM images were acquired using an Auriga cross-beam workstation dual column FIB-SEM (Carl Zeiss Microscopy, White Plains, NY, USA), with an initial trenching beam of 30 kV and 4 nA, and a final polishing beam of 30 kV and 50 pA. Figure 4 shows that the fabrication procedures used here resulted in high-density, laterally-uniform, well-adhered, crack-free, ~400 nm thick Mg_2SiO_4 films. The samples contained isolated, occasional pores ~65 nm in diameter intermittently distributed at the Mg_2SiO_4–MgO interface, but those were neither expected, nor observed, to impact the experiments.

Figure S3 shows Raman spectra of the Mg_2SiO_4 | MgO samples. Like the grazing angle XRD measurements of Figure S1, these Raman results confirmed that the PLD deposition conditions used here produced phase-pure, highly crystalline forsterite films.

In preparation for DAC loading, a ~3 mm × 4 mm fragment of a Mg_2SiO_4 | MgO sample was thinned to ~18 microns in thickness. As shown in Figure S4, during this thinning process, the Mg_2SiO_4 films were protected from water contamination by placing the Mg_2SiO_4 side of the sample against a stainless-steel piston that was subsequently used with a stainless-steel die to planarize the sample via wet hand polishing on P1200 grit SiC sandpaper. Before planarization, Crystalbond (Ted Pella; Redding, CA, USA) was used to bond all edges of the Mg_2SiO_4 | MgO fragments, but not their centers, to the stainless-steel piston. Once the desired sample thickness was achieved, tweezers were used to fracture the samples and remove portions that had not been in contact with the Crystalbond. After polishing, the Mg_2SiO_4 | MgO

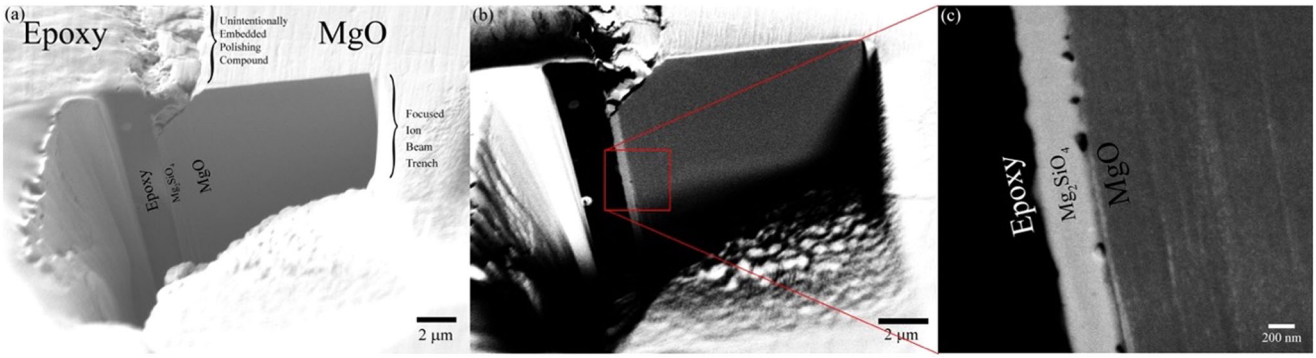

Fig. 4 Focused ion beam-scanning electron microscopy (FIB-SEM) cross sections. These cross sections in **a** secondary electron mode, and **b**, **c** back-scattered electron mode were performed on a fragment of the same 1473 K annealed Mg_2SiO_4 | MgO PLD sample that was used to produce all the DAC-loaded Mg_2SiO_4 | MgO fragments reported here. EDS point scans confirmed the compositions listed in the figure.

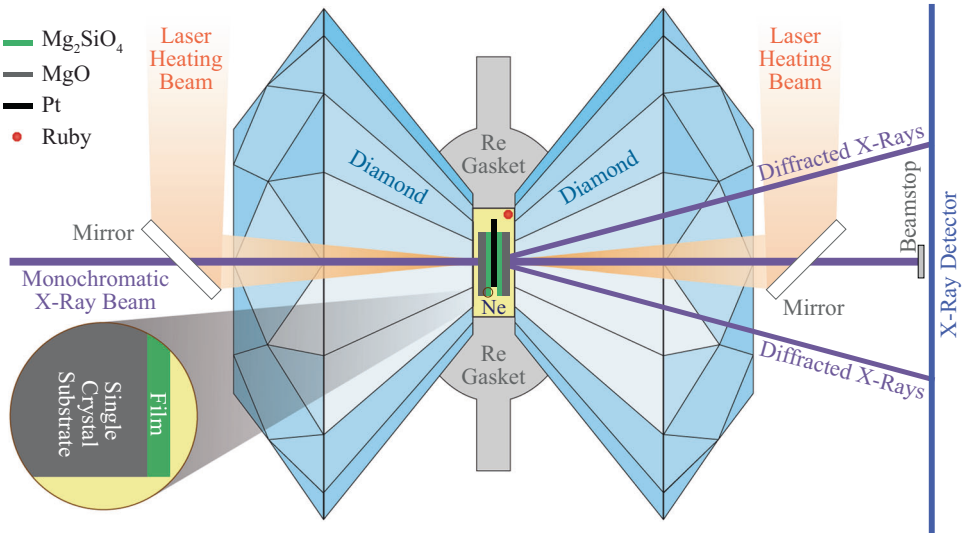

Fig. 5 Schematic of the DAC-loaded thin film experimental setup. Here, a piece of platinum is sandwiched between two opposing Mg_2SiO_4 | MgO samples within a laser-heated, neon-gas-loaded diamond anvil cell. The interrogating X-ray beam enters on the left and is detected on the right. Not drawn to scale.

fragments were stored in non-hermetic plastic containers. Sample fragments were then loaded into a standard DAC equipped with 300 μm culet diamonds, as shown schematically in Fig. 5. The Re DAC gaskets used here were pre-indented to ~30 μm and laser-drilled to provide a 150-μm-sized sample chamber. During loading, Pt foil was placed between two opposing Mg_2SiO_4 | MgO samples pieces, such that the films side of each fragment faced the Pt foil, which enabled laser heating from both sides of the DAC. Laser heated lasted between 15–20 min, depending on the highest temperature reached and number of measurements taken at each pressure point. The Pt also served as a pressure marker at high temperatures. A ruby fragment placed near the sample served as a pressure marker at room temperature. To enable pressure transmission, the DAC was loaded with Ne gas.

In situ synchrotron XRD measurements on the DAC-loaded thin film samples were then performed up to 26.5 GPa and 2300 K at the 13-IDD and 13-BMC beamlines of the Advanced Photon Source (APS). At the 13-BMC beamline, a monochromatic X-ray beam (28.6 keV, $\lambda = 0.434$ Å) was focused down to 12 (H) × 18 (V) μm^2. At the 13-IDD beamline, a monochromatic X-ray beam (37 keV, $\lambda = 0.3344$ Å) was focused on a spot of 4 (H) × 3 (V) μm^2 while a double-sided laser heating beam (100 W, $\lambda = 1064$ nm) was focused to a ~10 μm diameter spot on the sample[77]. In the first APS analysis session, labeled Run #1 and conducted in October of 2022 at 13-IDD, pressure was first increased to 13.5 GPa and XRD measurements were taken before, during, and after laser heating the sample. This procedure was repeated, on a different portion of the sample, after the pressure was increased to 23.5 GPa. In the second APS analysis session, labeled Run #2 and conducted in March 2023 at 13-IDD, temperature-dependent XRD measurements were taken at 9.5, 11.5, 18.0, and 19.5 GPa using the same procedures as in Run #1. In the third APS analysis session, labeled Run #3 and performed in April 2023 at 13-BMC, XRD measurements were taken at 300 K up to 26.5 GPa without laser heating. Due to a weaker thin film signal intensity observed in the Run #2 sample compared to the Run #1 sample, as shown in Fig. 2 the elevated temperature two-theta XRD patterns were stacked over certain temperature ranges to improve the signal-to-noise ratio. Unfortunately, low film XRD signal-to-noise ratios, the low angular openings of the DACs used here, and the non-spherical diamond anvils used here prevented reliable and complete XRD characterization of the in situ anisotropic film strain, anisotropic film stress, and film crystallographic orientation distribution. Figure S5 shows the DAC loadings and synchrotron XRD point scan locations used here. The elevated temperature XRD analyzes were only performed in locations where the Mg_2SiO_4 | MgO sample overlapped the Pt laser absorber. All synchrotron-collected XRD data was

processed with Dioptas[78] and the diffraction patterns were indexed with PDIndexer, allowing for the Pt volume to be determined. Figure S6 shows (1) calibration of the ruby fluorescence peak position used for room temperature pressure measurement, and (2) calibration of the Pt volume used for room temperature and elevated temperature pressure measurement. The ruby fluorescence method relied on comparing the shift in the fluorescence wavelength to a calibration curve[79] that related the wavelength shift to the pressure. The pressure-volume-temperature equation of state of Pt[80] was solved to determine the DAC pressure according to the measured volume of the sample at a given temperature.

Data availability

The dataset used to generate Figs. 2 and 3 can be found at https://doi.org/10.5061/dryad.66t1g1k7x[81].

Received: 25 October 2023; Accepted: 22 January 2024;
Published online: 08 February 2024

References

1. Ringwood, A. E. The olivine–spinel transition in the earth's mantle. *Nature* **178**, 1303–1304 (1956).
2. Ringwood, A. E. Phase-transformations and their bearing on the constitution and dynamics of the mantle. *Geochim. Cosmochim. Acta* **55**, 2083–2110 (1991).
3. Bernal, J. D. & Jeffreys, H. Discussion of the paper "The strucuture of the Earth down to the 20° discontinuity". *Observatory: A Monthly Rev. Astron.* **59**, 267–268 (1936).
4. Zhao, D. Big mantle wedge, anisotropy, slabs and earthquakes beneath the Japan Sea. *Phys. Earth Planet. Inter.* **270**, 9–28 (2017).
5. Jiang, G., Zhao, D. & Zhang, G. Detection of metastable olivine wedge in the western Pacific slab and its geodynamic implications. *Phys. Earth Planet. Inter.* **238**, 1–7 (2015).
6. Kawakatsu, H. & Yoshioka, S. Metastable olivine wedge and deep dry cold slab beneath Southwest Japan. *Earth Planet. Sci. Lett.* **303**, 1–10 (2011).
7. Green, H. W., Chen, W. P. & Brudzinski, M. R. Seismic evidence of negligible water carried below 400-km depth in subducting lithosphere. *Nature* **467**, 828–831 (2010).
8. Grand, S. P. Mantle shear–wave tomography and the fate of subducted slabs. *Philos. Trans. R. Soc. Lond. A: Math., Phys. Eng. Sci.* **360**, 2475–2491 (2002).
9. Iidaka, T. & Furukawa, Y. Double seismic zone for deep earthquakes in the izu-bonin subduction zone. *Science* **263**, 1116–1118 (1994).
10. Wiens, D. A., McGuire, J. J. & Shore, P. J. Evidence for transformational faulting from a deep double seismic zone in Tonga. *Nature* **364**, 790–793 (1993).
11. Burnley, P. C., Green, H. W. & Prior, D. J. Faulting associated with the olivine to spinel transformation in Mg_2GeO_4 and its implications for deep-focus earthquakes. *J. Geophys. Res.-Solid Earth Planets* **96**, 425–443 (1991).
12. Kirby, S. H., Durham, W. B. & Stern, L. A. Mantle phase changes and deep-earthquake faulting in subducting lithosphere. *Science* **252**, 216–225 (1991).
13. Kubo, T., Ohtani, E., Kato, T., Shinmei, T. & Fujino, K. Effects of water on the α-β transformation kinetics in San Carlos olivine. *Science* **281**, 85–87 (1998).
14. Du Frane, W. L., Sharp, T. G., Mosenfelder, J. L. & Leinenweber, K. Ringwoodite growth rates from olivine with ~75 ppmw H_2O: metastable olivine must be nearly anhydrous to exist in the mantle transition zone. *Phys. Earth Planet. Inter.* **219**, 1–10 (2013).
15. Hosoya, T., Kubo, T., Ohtani, E., Sano, A. & Funakoshi, K.-I. Water controls the fields of metastable olivine in cold subducting slabs. *Geophys. Res. Lett.* **32**, https://doi.org/10.1029/2005GL023398 (2005).
16. Perrillat, J. P. et al. Mechanism and kinetics of the a-b transition in San Carlos olivine $Mg_{1.8}Fe_{0.2}SiO_4$. *J. Geophys. Res.-Solid Earth* **118**, 110–119 (2013).
17. Madon, M. & Poirier, J. P. Transmission electron microscope observation of alpha, beta, and gamma $(Mg,Fe)_2SiO_4$ in shocked meteorites- planar defects and polymorphic transitions. *Phys. Earth Planet. Inter.* **33**, 31–44 (1983).
18. Tomioka, N. & Okuchi, T. A new high-pressure form of Mg_2SiO_4 highlighting diffusionless phase transitions of olivine. *Sci. Rep.* **7**, 17351 (2017).
19. Kerschhofer, L., Sharp, T. G. & Rubie, D. C. Intracrystalline transformation of olivine to wadsleyite and ringwoodite under subduction zone conditions. *Science* **274**, 79–81 (1996).
20. Wu, T. C., Bassett, W. A., Burnley, P. C. & Weathers, M. S. Shear-promoted phase-transitions in Fe_2SiO_4 and Mg_2SiO_4 and the mechanism of deep earthquakes. *J. Geophys. Res.-Solid Earth* **98**, 19767–19776 (1993).
21. Brearley, A. J., Rubie, D. C. & Ito, E. Mechanisms of the transformations between the a, b and g-polymorphs of Mg_2SiO_4 at 15 GPa. *Phys. Chem. Miner.* **18**, 343–358 (1992).
22. Dupas-Bruzek, C., Sharp, T. G., Rubie, D. C. & Durham, W. B. Mechanisms of transformation and deformation in $Mg_{1.8}Fe_{0.2}SiO_4$ olivine and wadsleyite under non-hydrostatic stress. *Phys. Earth Planet. Inter.* **108**, 33–48 (1998).
23. Burnley, P. C. & Green, H. W. Stress dependence of the mechanism of the olivine–spinel transformation. *Nature* **338**, 753–756 (1989).
24. Čížková, H., van Hunen, J. & van den Berg, A. Stress distribution within subducting slabs and their deformation in the transition zone. *Phys. Earth Planet. Inter.* **161**, 202–214 (2007).
25. Babeyko, A. Y. & Sobolev, S. V. High-resolution numerical modeling of stress distribution in visco-elasto-plastic subducting slabs. *Lithos* **103**, 205–216 (2008).
26. Yang, T., Gurnis, M. & Zhan, Z. W. Trench motion-controlled slab morphology and stress variations: implications for the isolated 2015 Bonin Islands deep earthquake. *Geophys. Res. Lett.* **44**, 6641–6650 (2017).
27. Herwegh, M. & Kunze, K. The influence of nano-scale second-phase particles on deformation of fine grained calcite mylonites. *J. Struct. Geol.* **24**, 1463–1478 (2002).
28. Rosa, A. D. et al. Evolution of grain sizes and orientations during phase transitions in hydrous Mg_2SiO_4. *J. Geophys. Res. Solid Earth* **121**, 7161–7176 (2016).
29. Sharp, T. G., Bussod, G. Y. A. & Katsura, T. Microstructures in b-$Mg_{1.8}Fe_{0.2}SiO_4$ experimentally deformed at transition-zone conditions. *Phys. Earth Planet. Inter.* **86**, 69–83 (1994).
30. Demouchy, S. et al. Forsterite to wadsleyite phase transformation under shear stress and consequences for the Earth's mantle transition zone. *Phys. Earth Planet. Inter.* **184**, 91–104 (2011).
31. Ohuchi, T. et al. In situ X-ray and acoustic observations of deep seismic faulting upon phase transitions in olivine. *Nat. Commun.* **13**, 5213 (2022).
32. Levchenko, A. A., Li, G., Boerio-Goates, J., Woodfield, B. F. & Navrotsky, A. TiO_2 stability landscape: polymorphism, surface energy, and bound water energetics. *Chem. Mater.* **18**, 6324–6332 (2006).
33. Luttrell, T. et al. Why is anatase a better photocatalyst than rutile?—Model studies on epitaxial TiO_2 films. *Sci. Rep.* **4**, 4043 (2014).
34. Žerjav, G., Žižek, K., Zavašnik, J. & Pintar, A. Brookite vs. rutile vs. anatase: what's behind their various photocatalytic activities? *J. Environ. Chem. Eng.* **10**, 107722 (2022).
35. Zhao, Z. et al. Grain-size effects on the ferroelectric behavior of dense nanocrystalline $BaTiO_3$ ceramics. *Phys. Rev. B* **70**, 024107 (2004).
36. Uchino, K., Sadanaga, E. & Hirose, T. Dependence of the crystal structure on particle size in barium titanate. *J. Am. Ceram. Soc.* **72**, 1555–1558 (1989).
37. Tsunekawa, S. et al. Critical size and anomalous lattice expansion in nanocrystalline $BaTiO_3$ particles. *Phys. Rev. B* **62**, 3065–3070 (2000).
38. DeHoff, R. *Thermodynamics in Materials Science*. 2nd edn, 409–442 (CRC Press, 2006).
39. Young, T. An essay on the cohesion of fluids. *Philos. Trans. R. Soc. Lond.* **95**, 65–87 (1805).
40. Laplace, P. S. M. D. *Traité de Mécanique Céleste*. Vol. 4, 1–79 (Courcier, 1805).
41. Bruno, M. et al. Ab initio calculations of the main crystal surfaces of forsterite (Mg_2SiO_4): a preliminary study to understand the nature of geochemical processes at the olivine interface. *J. Phys. Chem. C.* **118**, 2498–2506 (2014).
42. Mao, H. K., Xu, J. & Bell, P. M. Calibration of the ruby pressure gauge to 800 kbar under quasi-hydrostatic conditions. *J. Geophys. Res.-Solid Earth Planets* **91**, 4673–4676 (1986).
43. Ohring, M. *The Materials Science of Thin Films*, 2nd edn, 1–794 (Academic Press, 2002).
44. Fluri, A., Pergolesi, D., Roddatis, V., Wokaun, A. & Lippert, T. In situ stress observation in oxide films and how tensile stress influences oxygen ion conduction. *Nat. Commun.* **7**, 10692 (2016).
45. Prinz, G. A. Stabilization of BCC Co via epitaxial growth on GaAs. *Phys. Rev. Lett.* **54**, 1051–1054 (1985).
46. Proffit, D. L. et al. Phase stabilization of d-Bi_2O_3 nanostructures by epitaxial growth onto single crystal $SrTiO_3$ or $DyScO_3$ substrates. *Appl. Phys. Lett.* **96**, 021905 (2010).
47. Chen, Y. et al. Strain engineering and epitaxial stabilization of halide perovskites. *Nature* **577**, 209–215 (2020).
48. Straley, E. M., Dorfman, S. M. & Nicholas, J. D. Correlation between the wafer curvature and fluorescence of pulsed laser deposited ruby thin films stressed to ~2 GPa. *J. Appl. Phys.* **125**, 245904 (2019).
49. Santerre, F., El Khakani, M. A., Chaker, M. & Dodelet, J. P. Properties of TiC thin films grown by pulsed laser deposition. *Appl. Surf. Sci.* **148**, 24–33 (1999).
50. Freund, L. B. & Suresh, S. *Thin Film Materials: Stress, Defect Formation and Surface Evolution*. 1–770 (Cambridge University Press, 2003).

51. Miura, H., Ohta, H., Okamoto, N. & Kaga, T. Crystallization-induced stress in silicon thin films. *Appl. Phys. Lett.* **60**, 2746–2748 (1992).
52. Dorfman, S. M. et al. Control of deviatoric stress in the diamond anvil cell through thermal expansion mismatch stress in thin films. *Phys. Chem. Miner.* **49**, 16 (2022).
53. Dohmen, R., Becker, H. W., Meissner, E., Etzel, T. & Chakraborty, S. Production of silicate thin films using pulsed laser deposition (PLD) and applications to studies in mineral kinetics. *Eur. J. Mineral.* **14**, 1155–1168 (2002).
54. Wang, Q., Liu, C., Han, Y., Gao, C. & Ma, Y. The determination of ionic transport properties at high pressures in a diamond anvil cell. *Rev. Sci. Instrum.* **87**, 123904 (2016).
55. Fasaki, I., Koutoulaki, A., Kompitsas, M. & Charitidis, C. Structural, electrical and mechanical properties of NiO thin films grown by pulsed laser deposition. *Appl. Surf. Sci.* **257**, 429–433 (2010).
56. Raju, N. R. C., Kumar, K. J. & Subrahmanyam, A. Physical properties of silver oxide thin films by pulsed laser deposition: effect of oxygen pressure during growth. *J. Phys. D Appl. Phys.* https://doi.org/10.1088/0022-3727/42/13/135411 (2009).
57. Moholkar, A. V. et al. Synthesis and characterization of Cu_2ZnSnS_4 thin films grown by PLD: solar cells. *J. Alloy. Compd.* **509**, 7439–7446 (2011).
58. Fallon, P. J. et al. Properties of filtered-ion-beam-deposited diamond-like carbon as a function of ion energy. *Phys. Rev. B* **48**, 4777–4782 (1993).
59. Dubrovinskaia, N. et al. Terapascal static pressure generation with ultrahigh yield strength nanodiamond. *Sci. Adv.* **2**, e1600341 (2016).
60. Irifune, T., Kunimoto, T., Shinmei, T. & Tange, Y. High pressure generation in Kawai-type multianvil apparatus using nano-polycrystalline diamond anvils. *C R Geosci.* **351**, 260–268 (2019).
61. Hernandez, E. R., Brodholt, J. & Alfe, D. Structural, vibrational and thermodynamic properties of Mg_2SiO_4 and $MgSiO_3$ minerals from first-principles simulations. *Phys. Earth Planet. Inter.* **240**, 1–24 (2015).
62. Jacobs, M. H. G., Schmid-Fetzer, R. & Berg, A. P. V. D. Phase diagrams, thermodynamic properties and sound velocities derived from a multiple Einstein method using vibrational densities of states: an application to MgO–SiO_2. *Phys. Chem. Miner.* **44**, 43–62 (2017).
63. Katsura, T. et al. Olivine-wadsleyite transition in the system $(Mg,Fe)_2SiO_4$. *J. Geophys. Res.: Solid Earth* **109**, B02209 (2004).
64. Akaogi, M., Ito, E. & Navrotsky, A. Olivine-modified spinel-spinel transitions in the system Mg_2SiO_4-Fe_2SiO_4: calorimetric measurements, thermochemical calculation, and geophysical application. *J. Geophys. Res.: Solid Earth* **94**, 15671–15685 (1989).
65. Chopelas, A. Thermal properties of β-Mg_2SiO_4 at mantle pressures derived from vibrational spectroscopy: implications for the mantle at 400 km depth. *J. Geophys. Res.: Solid Earth* **96**, 11817–11829 (1991).
66. Suito, K. in *High Pressure Research: Applications in Geophysics* (eds Manghani, M. H. & Akimoto, S.) 255–266 (San Diego, 1977).
67. Morishima, H. et al. The phase-boundary between a-Mg_2SiO_4 and B-Mg_2SiO_4 determined by in situ X-ray observation. *Science* **265**, 1202–1203 (1994).
68. Suzuki, A. et al. In situ determination of the phase boundary between Wadsleyite and Ringwoodite in Mg_2SiO_4. *Geophys. Res. Lett.* **27**, 803–806 (2000).
69. Inoue, T. et al. The phase boundary between Wadsleyite and Ringwoodite in Mg_2SiO_4 determined by in situ X-ray diffraction. *Phys. Chem. Miner.* **33**, 106–114 (2006).
70. Chanyshev, A. et al. Depressed 660-km discontinuity caused by Akimotoite–Bridgmanite transition. *Nature* **601**, 69–73 (2022).
71. Ito, E. & Takahashi, E. Postspinel transformations in the system Mg_2SiO_4-Fe_2SiO_4 and some geophysical implications. *J. Geophys. Res.-Solid Earth Planets* **94**, 10637–10646 (1989).
72. Fei, Y. et al. Experimentally determined postspinel transformation boundary in Mg_2SiO_4 using MgO as an internal pressure standard and its geophysical implications. *J. Geophys. Res.-Solid Earth* **109**, B02305 (2004).
73. Kubo, T. et al. Formation of metastable assemblages and mechanisms of the grain-size reduction in the postspinel transformation of Mg_2SiO_4. *Geophys. Res. Lett.* **27**, 807–810 (2000).
74. Cottaar, S. & Deuss, A. Large-scale mantle discontinuity topography beneath Europe: signature of akimotoite in subducting slabs. *J. Geophys. Res.: Solid Earth* **121**, 279–292 (2016).
75. Katsura, T. et al. Thermal expansion of forsterite at high pressures determined by in situ X-ray diffraction: the adiabatic geotherm in the upper mantle. *Phys. Earth Planet. Inter.* **174**, 86–92 (2009).
76. Kubicek, M. et al. Electrochemical properties of $La_{0.6}Sr_{0.4}CoO_{3-\delta}$ thin films investigated by complementary impedance spectroscopy and isotope exchange depth profiling. *Solid State Ion.* **256**, 38–44 (2014).
77. Prakapenka, V. B. et al. Advanced flat top laser heating system for high pressure research at GSECARS: application to the melting behavior of germanium. *High. Press. Res.* **28**, 225–235 (2008).
78. Prescher, C. & Prakapenka, V. B. DIOPTAS: a program for reduction of two-dimensional X-ray diffraction data and data exploration. *High. Press. Res.* **35**, 223–230 (2015).
79. Dewaele, A., Torrent, M., Loubeyre, P. & Mezouar, M. Compression curves of transition metals in the Mbar range: experiments and projector augmented-wave calculations. *Phys. Rev. B* **78**, 104102 (2008).
80. Fei, Y. et al. Toward an internally consistent pressure scale. *PNAS* **104**, 9182–9186 (2006).
81. Berrada, M. et al. Dataset for detection of thin film phase transformations at high-pressure and high-temperature in a diamond anvil cell. *Dryad.* https://doi.org/10.5061/dryad.66t1g1k7x (2023).
82. Smyth, J. R. & Hazen, R. M. The crystal structures of forsterite and hortonolite at several temperatures up to 900 °C. *Am. Miner* **58**, 588–593 (1973).
83. Hazen, R. M., Weinberger, M. B., Yang, H. & Prewitt, C. T. Comparative high-pressure crystal chemistry of wadsleyite, b-$(Mg_{1-x}Fe_x)_2SiO_4$, with x=0 and 0.25. *Am. Miner.* **85**, 770–777 (2000).
84. Sasaki, S., Prewitt, C. T., Sato, Y., Ito, E. & Single-Crystal, X. Ray study of gamma Mg_2SiO_4. *Am. Miner* **87**, 7829–7832 (1982).
85. Horiuchi, H., Hirano, M., Ito, E. & Matsui, Y. $MgSiO_3$ (ilmenite-type): single crystal X-ray diffraction study. *Am. Miner* **67**, 788–793 (1982).
86. Sugahara, M. et al. Reinvestigation of the $MgSiO_3$ perovskite structure at high pressure. *Am. Miner.* **91**, 533–536 (2006).
87. Wyckoff, R. W. G. *Crystal Structures* Volume 1, 2nd edn (Interscience Publishers, 1963).
88. de Smedt, J., Keesom, W. H. & Mooy, H. H. On the crystal structure of neon. in *Proceedings of the Koninklijke Nederlandse Akademie van Wetenschappen* Vol. 33, 255–257 (1930).
89. Hazen, R. M. Effects of temperature and pressure on the cell dimension and X-ray temperature factors of periclase. *Am. Miner.* **61**, 266–271 (1976).
90. Ishii, T., Kojitani, H. & Akaogi, M. Post-spinel transitions in pyrolite and Mg_2SiO_4 and akimotoite–perovskite transition in $MgSiO_3$: precise comparison by high-pressure high-temperature experiments with multi-sample cell technique. *Earth Planet. Sci. Lett.* **309**, 185–197 (2011).
91. Irifune, T. et al. The postspinel phase boundary in Mg_2SiO_4 determined by in situ X-ray diffraction. *Science* **279**, 1698–1700 (1998).
92. Presnall, D. C. & Walter, M. J. Melting of forsterite, Mg_2SiO_4, from 9.7 to 16.5 GPa. *J. Geophys. Res.: Solid Earth* **98**, 19777–19783 (1993).
93. Katsura, T. et al. Post-spinel transition in Mg_2SiO_4 determined by high P-T in situ X-ray diffractometry. *Phys. Earth Planet. Inter.* **136**, 11–24 (2003).
94. Ghosh, S. et al. Effect of water in depleted mantle on post-spinel transition and implication for 660 km seismic discontinuity. *Earth Planet. Sci. Lett.* **371-372**, 103–111 (2013).
95. de Koker, N. P., Stixrude, L. & Karki, B. B. Thermodynamics, structure, dynamics, and freezing of Mg_2SiO_4 liquid at high pressure. *Geochim. Cosmochim. Acta* **72**, 1427–1441 (2008).
96. De Koker, N. & Stixrude, L. Self-consistent thermodynamic description of silicate liquids, with application to shock melting of MgO periclase and $MgSiO_3$ perovskite. *Geophys. J. Int.* **178**, 162–179 (2009).
97. Litasov, K. et al. Water solubility in Mg-perovskites, and water storage capacity in the lower mantle. *Earth Planet. Sci. Lett.* **211**, 189–203 (2003).

Acknowledgements

This work was funded via National Science Foundation awards EAR-2031149 (J.D.N.), EAR-2031331 (J.L.), EAR-1829273 (B.C.), and EAR-2127807 (B.C.). PLD film growth was conducted by D. Bruce Buchholz at the Materials Research Center at Northwestern University, which is supported by the National Science Foundation MRSEC program (DMR-1720139) and the Soft and Hybrid Nanotechnology Experimental (SHyNE) Resource (NSF EECS-2025633). Focused ion beam-scanning electron microscopy was conducted with help from Per Askeland at the Michigan State University Composite Materials and Resource Center, which is supported by the NSF Major Research Instrumentation Program (NSF-MRI-0922999) and Michigan State University. Work conducted at 13-BMC through the Partnership for Extreme Crystallography (PX^2) was supported by COMPRES under NSF Cooperative Agreement EAR-1661511 and by GSECARS. Use of the COMPRES-GSECARS gas loading system was supported by COMPRES under NSF Cooperative Agreement EAR-1661511 and by GSECARS through NSF grant EAR-1634415. This research used resources of the Advanced Photon Source; a U.S. Department of Energy (DOE) Office of Science user facility operated for the DOE Office of Science by Argonne National Laboratory under Contract No. DE-AC02-06CH11357.

Author contributions

Conceptualization: J.D.N., J.L., and B.C. Methodology: J.D.N., J.L., and B.C. Investigation: M.B., D.Zhou, S.W., G.H., B.C., J.L., and J.D.N. Visualization: M.B. and J.D.N. Supervision: B.C., J.D.N., J.L., S.C., V.P., P.Q.H.N., and D.Zhang. Writing: J.D.N., M.B., J.L., and B.C.

Funding
Open Access funding enabled and organized by Projekt DEAL.

Competing interests
The authors declare no competing interests.

Additional information
Supplementary information The online version contains supplementary material available at https://doi.org/10.1038/s43247-024-01234-9.

Correspondence and requests for materials should be addressed to Jason D. Nicholas.

Peer review information *Communications Earth & Environment* thanks the anonymous reviewers for their contribution to the peer review of this work. Primary Handling Editor: Joe Aslin. A peer review file is available.